



OPEN

SUBJECT AREAS:

NANOPHOTONICS AND
PLASMONICS

SUB-WAVELENGTH OPTICS

Received
29 April 2014Accepted
8 July 2014Published
1 August 2014Correspondence and
requests for materials
should be addressed to
J.Z. (jszhang@pku.
edu.cn)

Ultra-broadband and efficient surface plasmon polariton launching through metallic nanoslits of subwavelength period

Guangyuan Li¹ & Jiasen Zhang^{1,2}¹State Key Laboratory for Mesoscopic Physics, Department of Physics, Peking University, Beijing 100871, China, ²Collaborative Innovation Center of Quantum Matter, Beijing 100871, China.

Ultra-broadband, efficient and unidirectional surface plasmon polariton (SPP) launching is of great concern in plasmonic devices and circuits. To address this challenge, a novel method adopting deep-subwavelength slits of subwavelength period ($\lambda_{\text{SPP}}/4 \sim \lambda_{\text{SPP}}/3$) in a thick metal film and under backside illumination is proposed. A new band pattern featuring broadband and wide angular characteristics, which is due to the coupling of the zeroth-order SPP resonance at the superstrate–metal interface and the first-order SPP resonance at the metal–substrate interface, is observed for the first time in the dispersion diagram. Unidirectional SPP launching efficiency of $\sim 50\%$, ultra-broad bandwidth of up to 780 nm, covering the entire optical fiber communication bands, and relatively wide angular range of 7° are achieved. This remarkable efficient, ultra-broadband and wide angular performance is demonstrated by carefully designed experiments in the near infrared regime, showing good agreement with numerical results.

As a promising candidate to provide the new generation information network with improved bandwidth and speed¹, plasmonics has generated increasing research enthusiasms. The last decade has witnessed remarkable progress in the development of plasmonics and its applications in areas such as light routing and manipulation at the nanoscale^{2–4}, especially the wavelength division multiplexing (WDM) plasmonic circuit elements, such as the plasmonic demultiplexers^{5,6}, broadband modulators⁷, and broadband antennas⁸.

In order to investigate the WDM plasmonic circuits, there is a prerequisite that broadband surface plasmon polaritons (SPPs) propagating in a well-defined direction should be efficiently launched with appropriate approaches. Although various configurations have been proposed and continuous efforts have been exerted to establish the theory and optimize the structure, it remains challenging to realize unidirectional, efficient and meanwhile broadband SPP launching. The conventional prism approach making use of attenuated total reflection (ATR), known as the Kretschmann-Raether configuration, is very sensitive to the wavelength and the angle of incidence⁹, making it widely used in sensors. Conversely, SPP launching approaches based on one or two subwavelength features (such as slits, grooves or ridges) in or on a thick metal film^{10–17} may be angular insensitive or even relatively broadband. However, as pointed out in refs. 12 and 18, the launching efficiency (usually not reported) is rather small. It has been widely accepted that efficient and practical SPP launchers should employ periodic or aperiodic arrays of scattering objects¹². For conventional periodic gratings, the unidirectional SPP launching efficiency is limited although continuous efforts have been put on the geometrical optimization^{19–23}. Recently, the depths, the widths, and the neighboring distances of aperiodic grooves have been so carefully optimized that $\sim 50\%$ launching efficiency in the desired direction has been theoretically^{24,25} and experimentally¹⁸ achieved. With aperiodic metallic grooves, a record unidirectional extinction ratio of 55 has also been reported²⁶, but the coupling efficiency was not provided. More recently, the broadband and unidirectional excitation of SPPs has been achieved using chirped plasmonic gratings⁸, however the launching efficiency (not reported) is supposedly small compared with their periodic counterparts. In other words, the SPP launching in these periodic or aperiodic metallic gratings suffers from very limited spectral bandwidth (only a few dozens of nanometers) in case of high efficiency, or very low coupling efficiency in case of broad bandwidth, restricting their applications in WDM plasmonic circuits. A probable reason is that the periods or neighboring distances were usually restricted to be comparable with or larger than the SPP wavelengths.



In order to achieve high unidirectional efficiency and simultaneously ultra-broad bandwidth of more than 415 nm so as to cover the entire optical fiber communication bands (O, E, S, C, L, and U bands), in this work, we propose a novel SPP launching method using periodic deep-subwavelength slits of subwavelength period ($\lambda_{\text{SPP}}/4 \sim \lambda_{\text{SPP}}/3$), where λ_{SPP} is the SPP wavelength. The slits are milled in an optically thick metal film and obliquely illuminated from the back side, prohibiting the incident light from becoming significant source of noise and reducing the system's size¹⁰. Interestingly, for the first time we find a new band pattern featuring broadband and wide angular characteristics, which is due to the coupling of the zeroth-order SPP resonance at the superstrate–metal interface and the first-order SPP resonance at the metal–substrate interface. The corresponding unidirectional SPP launching efficiency is found to be $\sim 50\%$ over an ultra-broadband range (up to 780 nm) and relatively large angular range ($\sim 7^\circ$). This remarkable performance makes the proposed SPP launching approach distinct from conventional periodic or aperiodic metallic gratings, of which periods or neighboring distances are usually comparable with or larger than the SPP wavelengths, featuring spectrally and angularly sensitive SPP launching efficiencies^{18,24,26}. It is experimentally demonstrated in the near-infrared regime.

Results

The configuration in Fig. 1(a) illustrates N periodic slits of deep-subwavelength width w and subwavelength period p in an optically-thick metal film of thickness h . The slits are back-side illuminated by a transverse-magnetic polarized light of oblique incidence angle θ . This structure is distinct from the Kretschmann–Raether configuration⁹ because of the slit array and the optically thick metal film. It also differs from conventional metallic gratings because p is much smaller than the SPP wavelength.

We firstly calculate the band structure of the corresponding one-dimensional (1D) plasmonic crystal, i.e. the fully-periodic ($N = \infty$) grating. To cover entire optical fiber communication bands (1260 nm \sim 1675 nm), we set $p = 440$ nm, which is about $\lambda_{\text{SPP}}/4 \sim \lambda_{\text{SPP}}/3$, $w = 100$ nm, and $h = 300$ nm (optically thick enough). Fig. 1(b) shows the ω – k_{\parallel} dispersion diagram, where ω is the angular frequency, $k_{\parallel} = k_0 n_{\text{sub}} \sin \theta$ is the in-plane wavevector of the incident light from the substrate. The color scale represents the absorption

intensity. As have been pointed out in refs. 27 and 28, there are narrow bright bands that generally follow two sets of curves: the folded dispersion relations of SPPs on flat metallic surfaces (black lines) and the Rayleigh anomaly (RA) wavelengths (red lines) at the Au–substrate interface (solid lines) and the superstrate–Au interface (dashed lines). The dispersion relations of SPPs are determined by the Bragg coupling condition²⁹,

$$k_0 \text{Re}(n_{\text{SPP,sub/sup}}) p - k_0 n_{\text{sub}} p \sin \theta = 2m_1 \pi, \quad (1)$$

where $n_{\text{SPP,sub/sup}} = \sqrt{\epsilon_m \epsilon_{\text{sub/sup}} / (\epsilon_m + \epsilon_{\text{sub/sup}})}$ is the effective index of SPP on flat metallic surface with $\epsilon_{\text{sub/sup}}$ being the relative permittivity of the substrate (sub) or superstrate (sup), and m_1 is the diffraction order. The RA wavelengths are defined by the passing-off of a diffraction order (m_2),

$$k_0 \epsilon_{\text{sub/sup}} p - k_0 n_{\text{sub}} p \sin \theta = 2m_2 \pi. \quad (2)$$

We should note that these narrow bands are observed for wavelengths comparable to the periods and the SPP and RA curves almost merge at small energies, for which $k_{\text{SPP}} \approx k_0$. These properties agrees well with previous studies on conventional metallic gratings^{27,28}, of which periods are comparable with or larger than the SPP wavelengths. These narrow bands explain why the SPP launching efficiencies of conventional metallic gratings are spectrally and angularly sensitive.

Interestingly, for the first time we observe a new bright band featuring large spectral and angular ranges. It locates between the 0th-order SPP resonance wavelength at the superstrate–Au interface, $\text{SPP}_{0,\text{sup}}$, and the first-order SPP resonance wavelength at the Au–substrate interface, $\text{SPP}_{1,\text{sub}}$. Its spectral and angular characteristic and location make it distinct from the above-mentioned narrow bands locates between the SPP and RA curves, as well as the slit Fabry-Perot (F-P) resonance curve determined by $2 k_0 \text{Re}(n_{s,\text{eff}}) h + \arg(r_{s,\text{top}}) + \arg(r_{s,\text{bot}}) = 2 \pi m_3$, where $n_{s,\text{eff}}$ is the effective index of the slit mode, $r_{s,\text{top}}$ and $r_{s,\text{bot}}$ are the reflectance coefficients of the slit mode at the top and bottom openings, respectively, the function “arg” refer to the argument of a complex number, and m_3 is an integer.

To further understand the physical origin of the new band, we theoretically calculate the SPP launching efficiency for N periodic

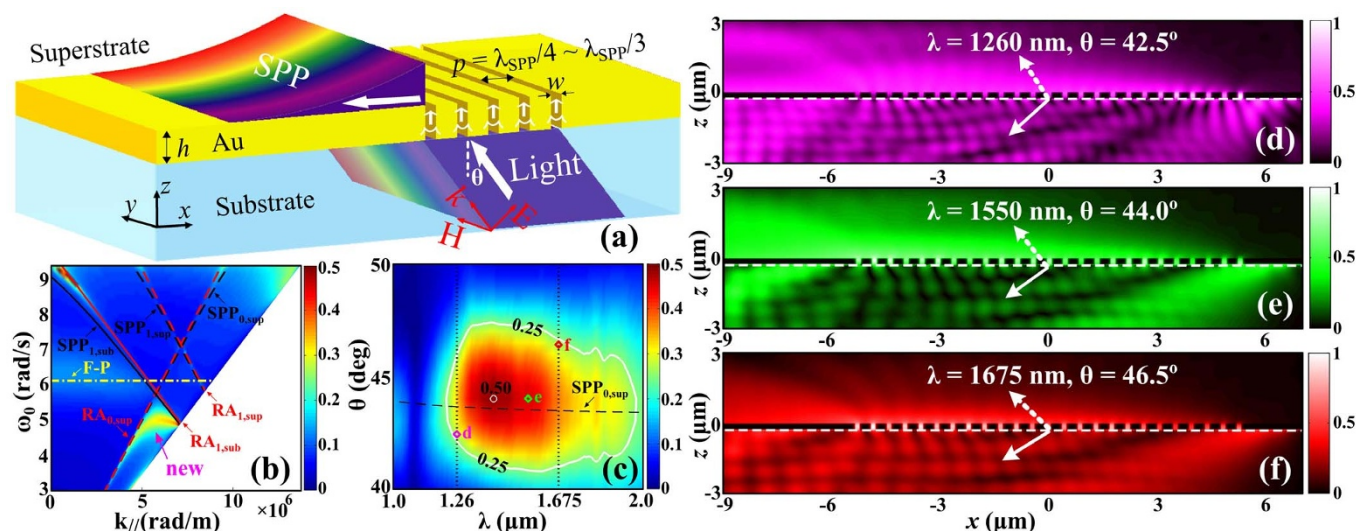


Figure 1 | (a) Schematic of the proposed SPP launching configuration. (b) Absorption diagram of the plasmonic crystal. (c) The spectral and angular dependence of η_c^+ for $N = 25$ with the white contour indicating half the optimal efficiency. (d)–(f) Near-field $|H_y|$ under various wavelengths and incidence angles as indicated by the diamonds in (c). The incident plane indicated by a dashed line locates at 100 nm below the quartz–metal interface. The dashed and solid arrows show incident direction and specular reflection direction, respectively. The calculations were performed with $h = 300$ nm, $w = 100$ nm, and $p = 440$ nm.

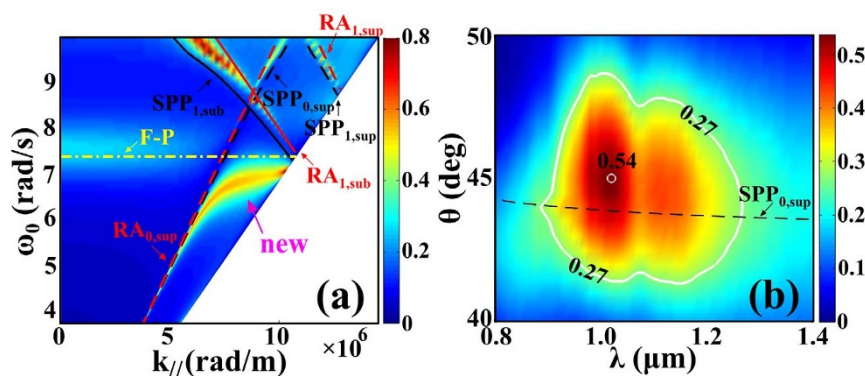


Figure 2 | (a) Absorption diagram of the plasmonic crystal. (b) Spectral and angular dependence of η_c^+ for $N = 25$. The calculations were performed with $h = 200$ nm, $w = 30$ nm, and $p = 290$ nm.

metallic slits, η_c^\pm , which is defined as the ratio of the power of the launched forward- (“+”) or backward-propagating (“−”) SPPs to that of the incident light over the whole grating length, $(N-1)p + w$. Fig. 1(c) shows the spectral and angular dependence of η_c^+ of $N = 25$. It reveals that η_c^+ reaches as large as 50% and holds more than 25% over extremely wide spectral range and relatively large angular ranges. An ultra-broad spectral full width at half maximum (FWHM) of up to 780 nm (from 1210 nm to 1990 nm) at $\theta = 44^\circ$ and an angular FWHM of 7° at $\lambda = 1550$ nm are achieved. The ultra-broad bandwidth covers the entire optical fiber communication bands, making the proposed SPP launching approach very promising in WDM plasmonic circuits. We note that η_c^+ is extremely small over the corresponding spectral and angular ranges, corresponding to large extinction ratio, which is defined as $E_R \equiv \eta_c^+ / \eta_c^-$ and more than 20 (see Fig. S1 in Supplementary Information). We also note that the spectral FWHM ranges of η_c^+ have been indicated by the location of the new band of the dispersion diagram in Fig. 1(b).

Given that the slit period of $\lambda_{SPP}/4 \sim \lambda_{SPP}/3$, if and only if $m_1 = 0$, Eq. (1) can be satisfied. In other words, only the 0^{th} -order SPP resonance exists for the transmitted diffraction. Each slit acts as a channel that converts the back-side incident light into SPPs propagating along the superstrate–metal interface (referred to as top-SPPs). SPPs propagating along the metal–air interface (referred to as bottom-SPPs) are also generated by the slits. Meanwhile, the launched top- and bottom-SPPs couple with each other through the slits and also re-radiate to the substrate because of Rayleigh-like scattering by the slit array³⁰. These re-radiated emissions interfere with the reflected diffraction field by the subwavelength metallic ridges, resulting in energy redistribution between the reflected field and launched top-SPPs in the transmitted field. In the dispersion diagram, the coupling of top-SPPs and bottom-SPPs will result in a band between their corresponding dispersion curves. In other words, the new band that locates between $SPP_{0,sup}$ and $SPP_{1,sub}$ in Fig. 1(b) should originate from the coupling of top-SPPs at the 0^{th} -order resonance and bottom-SPPs at the first-order resonance. On the other hand, the interference between SPP re-radiations and the metallic ridges’ reflected diffraction is vividly visualized by the near field distributions under various incident wavelengths and angles, as illustrated in Figs. 1(d)–1(f). The incident plane locates at 100 nm below the quartz–metal interface so as to manifest the reflected field. It is clearly shown that forward-propagating SPPs are launched efficiently while backward-propagating SPPs are very weak over the entire optical fiber communication bands and at various incident angles.

Since the new band locates between $SPP_{0,sup}$ and $SPP_{1,sub}$, it is possible to tune its location and accordingly the ultra-broad bandwidth of η_c^+ to the desired spectral range by varying $SPP_{0,sup}$ and $SPP_{1,sub}$, which are determined by structural parameters, such as p , n_{sup} and n_{sub} . By decreasing the geometrical parameters (p , w , and h),

the location of the new band is shifted to higher frequency, and accordingly the bandwidth of η_c^+ is blue-shifted. Fig. 2 shows the results for $h = 200$ nm, $w = 30$ nm, and $p = 290$ nm. Comparing Figs. 1(c) and 2(a), we observe that the spectral bandwidth has been blue-shifted from 1210 nm \sim 1990 nm to 890 nm \sim 1270 nm at $\theta = 44^\circ$ by reducing the slit period from $p = 440$ nm into $p = 290$ nm. It is worth to note that the slit period holds to be about $\lambda_{SPP}/4 \sim \lambda_{SPP}/3$. The blue-shift by decreasing geometrical size is in accordance with the scaling law³¹. Moreover, the angular FWHM is about 7° at $\lambda = 1000$ nm.

Note that the idea of the proposed SPP launcher originates from the dispersion properties of an infinite periodic array of slits, while the use of the SPP launcher should adopt a finite number N of slits so as to excite unidirectional SPPs on flat metallic surfaces. For conventional SPP launchers composed of periodic features with period comparable with λ_{SPP} , the SPP launching efficiencies depend on N ²³. This property also holds for the proposed SPP launcher with some differences. As shown in Fig. 3(a), η_c^+ first increases to about 51% and then decreases slowly as N increases. The decrease of η_c^+ is because the saturation of the launched SPPs due to scattering and propagation losses. Compared with conventional SPP launchers, which exhibit low η_c^+ and a rapid saturation of η_c^+ as N increases²³, the proposed SPP launching configuration is of much higher efficiency and much slower saturation. Fig. 3(a) also shows that the extinction ratio is larger than 100 if $N > 6$, indicating that the proposed configuration launches highly unidirectional SPPs. Comparing Figs. 1(c), 3(b) and 3(c), we notice that although the angular FWHM of the proposed SPP launcher decreases and the optimal efficiency varies as N increases, the ultra-broadband performance holds for various N . In other words, the efficient, unidirectional, ultra-broadband and relatively wide angular performance holds for the proposed SPP launchers of a very wide range of N . For the design of a SPP launcher of given N , the desired spectral ranges and the corresponding p , one may optimize w and h for the optimal efficiency using efficient theoretical models introduced in ref. 32.

To experimentally demonstrate the remarkable performance, we carefully designed samples composed of a launcher and a decoupler, as schematically shown in Fig. 4(a). Under back-side illumination of a TM-polarized light beam, forward-propagating top-SPPs are excited with a launching efficiency η_c^+ , and then scattered into far field by the decoupler with a decoupling efficiency η_d . The decoupling efficiency η_d is defined as the ratio of the re-radiated power P_O from the decoupler within a cone with a $\pm 30^\circ$ extraction angle, which is determined by the numerical aperture (NA) of the collecting microscope objective (NA = 0.5 here), to the power of top-SPPs at the slits. In Fig. 4(a), P_{IN} is the incident power onto the launcher.

Taking into account of the tunable wavelength range of the laser source we used in the experiment (800 nm to 920 nm) and the



fabrication yield, we designed the launcher of a sample, Launcher I, to be of the following parameters: $w = 60$ nm, $p = 240$ nm, and $N = 15$. The launcher of the other sample, Launcher II, has the following design parameters: $w = 120$ nm, $p = 480$ nm, and $N = 8$. Both launchers have the same slit length ($L = 54$ μm). Furthermore, the decouplers share the same parameters as Launcher II, except for the slit length $L/2$, because of two considerations: the noise power could be eliminated and the SPP coupling efficiency could be accurately inferred, as will be elaborated later. The scanning electron microscopy (SEM) images are shown in Figs. 4(b) to 4(d) (and Figs. S2(a)–(b) in Supplementary Information). From the calibrated SEM images, the measured slit parameters are determined with the average values and the standard derivations, which are obtained from statistics of slit widths and distances at different positions: $w = 55 \pm 15$ nm and $p = 248 \pm 15$ nm for Launcher I, $w = 105 \pm 6$ nm and $p = 495 \pm 7$ nm for Launcher II, and $w = 120 \pm 7$ nm and $p = 499 \pm 7$ nm for the decouplers.

With the optical setup schematically illustrated in Fig. 4(e), we obtained the images of the decoupler and Launcher I with a charge coupled device (CCD), as shown by Figs. 4(f) and 4(g), respectively. We note that the far-field reflection by Launcher I is significantly suppressed compared with the specular reflection by the surrounding flat metal surface, as predicted by the near-field distributions shown in Figs. 1(d)–1(f), although different parameters were used. The CCD images were further processed (see Methods) to accurately obtain the total launching-decoupling efficiency expressed as $\eta^+ = \eta_c^+ \eta_d \exp(-l/l_{\text{SPP}})$, where l_{SPP} is the SPP propagation length. We measured l_{SPP} adopting a method improved from the one introduced in ref. 33. Fig. 5 shows the structure design, a fabricated sample, the optical characterization and the image post-processing (see

Methods), and the measured results comparing with the theoretical values calculated using $l_{\text{SPP}} = 1/(2k_0 \text{Im}(n_{\text{SPP}}))$. The shorter-than-expected l_{SPP} in Fig. 5(d) is probably due to inelastic SPP scattering by the surface roughness inherently introduced during evaporated and increased by FIB patterning³³. To infer η_c^+ accurately from the measured $\eta^+ = \eta_c^+ \eta_d \exp(-l/l_{\text{SPP}})$, Launcher II and the decouplers are carefully designed so that an almost constant relationship exists between η_d and η_c^+ ($\text{II}, \theta = 45^\circ$), where II (or I) represents Launcher II (or Launcher I), over the laser wavelength range in our experiment, as shown in Fig. 6(a): $\eta_d \approx 1.19\eta_c^+$ ($\text{II}, \theta = 45^\circ$). The linear relationship holds for the fabricated samples, but it is slightly modified into $\eta_d \approx 1.17\eta_c^+$ ($\text{II}, \theta = 45^\circ$). As a result, we assume that this approximation also holds for the measured efficiencies and then infer η_c^+ and η_d from the measured η^+ as: $\eta_d \approx \sqrt{1.17\eta^+}$ ($\text{II}, \theta = 45^\circ$) $\exp(-l/l_{\text{SPP}})$ and η_c^+ (I/II) $\approx \eta^+$ (I/II)/ $\eta_d \exp(l/l_{\text{SPP}})$.

Figures 6(b) and 6(c) compare the experimental and the calculated η_c^+ of the two launchers with respect to λ for $\theta = 45^\circ$ and to θ for $\lambda = 830$ nm, respectively. Although the measured efficiencies are smaller than the calculated results, especially for Launcher I, they agree well in general trends. In Fig. 6(b), a slight oscillation occurs for the experimental data of Launcher I because of the interference between top-SPPs and bottom-SPPs at the decoupler, which should not appear in practical applications. Limited by the wavelength range of the laser source we used, we have only demonstrated the front part of the broadband and meanwhile efficient performance (see Supplementary Information) in the near infrared regime. In Fig. 6(c), the angular FWHM of more than 8° has been demonstrated experimentally.

Discussion

The difference between measured and calculated efficiencies in Figs. 6(b) and 6(c) could originate from the fabrication imperfections. As we have pointed previously, the measured slit parameters determined from the calibrated SEM images indicate that the fabrication deviations of Launcher I are relatively large. This is due to the large size of the whole sample and the deep-subwavelength slit width. Aside from the size deviations, some metallic ridges of Launcher I separate from the substrate because of extremely small widths (see Fig. 5(d)). However, even with these fabrication imperfections, all the measured η_c^+ (I) are larger than the measured slit duty factor (22.2%) across the laser wavelength range in the experiment for $\theta = 45^\circ$, and the maximum value is up to 31.9%.

Up to now, the largest efficiency of $\sim 52\%$ has been reported from a carefully optimized aperiodic SPP launcher¹⁸, which is illuminated from the top and sensitive to both λ and θ . As pointed out in ref. 10, the incident light from the top is a significant source of noise, unless directed away from a region of interest, which then decreases the signal and increases the system's size. This problem is eliminated using back-side illumination in optically thick metal films. Moreover, the neighboring distances of the aperiodic SPP launcher in ref. 18 is comparable to the SPP wavelength, whereas the period in our proposed method is of $\lambda_{\text{SPP}}/4 \sim \lambda_{\text{SPP}}/3$. As a result, the proposed SPP launching approach adopting back-side illumination and sub-wavelength period will also gain advantages in integration besides the attractive ultra-broadband and meanwhile efficient performance. Additionally, compared with aperiodic gratings^{8,18,24,26} of which the widths, the depths and the neighboring distances are different, the proposed periodic slits are much easier to fabricate.

In summary, we have proposed and demonstrated a novel method to realize unidirectional, efficient and meanwhile ultra-broadband SPP launching adopting deep-subwavelength metallic slits with period of $\lambda_{\text{SPP}}/4 \sim \lambda_{\text{SPP}}/3$. We expect that the proposed SPP launching method will be favorable in nanophotonic applications, especially WDM plasmonic circuits.

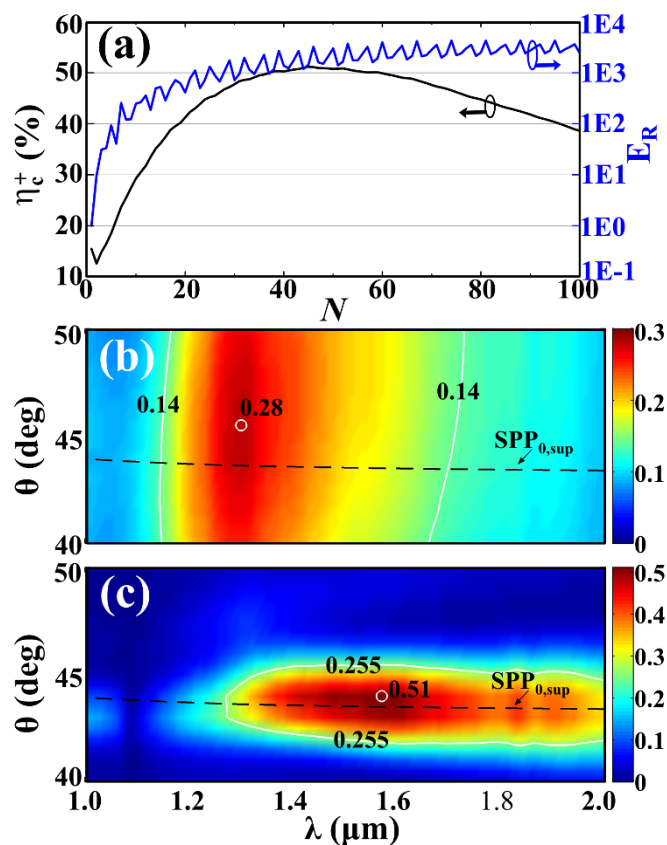


Figure 3 | (a) Dependence of η_c^+ and E_R on N . (b)(c) Spectral and angular dependence of η_c^+ for $N = 5$ (b) and $N = 50$ (c). The calculations were performed with $\lambda = 1550$ nm, $\theta = 44^\circ$, and other parameters (h , w , p) are the same as Fig. 1(c).

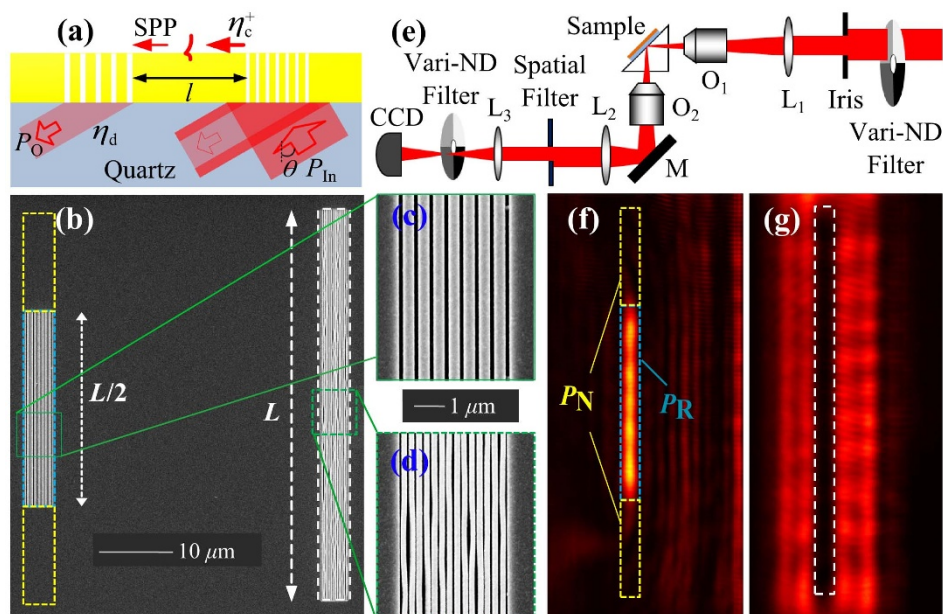


Figure 4 | (a) Schematic of the sample layout. (b)–(d) SEM images and close-ups of a sample composed of the decoupler and Launcher I. (e) Schematic of the optical characterization setup. (f)–(g) CCD images of the decoupler and Launcher I, respectively.

Methods

Simulation. The band structure of the 1D plasmonic crystal, the SPP launching efficiency η_c^\pm and decoupling efficiency η_d are calculated using the rigorous coupled wave analysis/aparic Fourier modal method (RCWA/a-FMM)^{34,35}. The near fields are calculated using Lumerical FDTD Solutions. The wavelength-dependent complex permittivities of gold are interpolated from experimental data³⁶, the superstrate and the material filling the slits are assumed to be air ($n_{\text{sup}} = 1.0$), and the refractive index of the substrate $n_{\text{sub}} = 1.46$ is used throughout this work.

Fabrication. A 200 nm-thick gold film is sputtered onto a 2 cm × 2 cm quartz substrate. A focused ion beam (FIB) milling system is used to mill samples composed

of a launcher and a decoupler with a separation distance l , and samples composed of a central slit and two surrounding grooves, all of which are 120 nm wide and separated with various pairs of asymmetric slit-groove distances (9, 12, 15, 21, 24, and 27 μm).

Characterization. The optical measurement is conducted using home-built experimental setups to obtain the CCD images. The light source is a continuous wave Ti:sapphire laser with a tunable wavelength range of 800 nm to 920 nm. The laser beam expanded by a telescope system and attenuated by a calibrated vari-ND filter illuminates a rectangle iris, which is imaged onto the launcher or the central slit from the substrate side using an imaging system composed of a lens L_1 and a microscope objective O_1 (50×, NA = 0.5). To measure the SPP coupling efficiency, the sample is

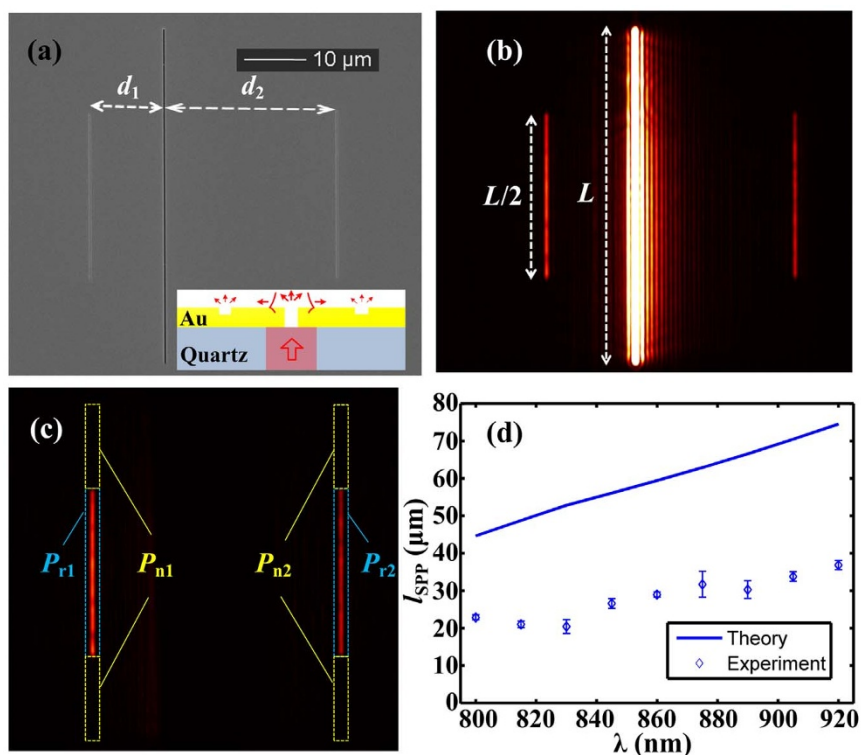


Figure 5 | (a) SEM image of a slit-groove doublet sample with $d_1 = 12 \mu\text{m}$ and $d_2 = 24 \mu\text{m}$. (b)(c) CCD images of the sample without and with the spatial filtering system, respectively. (d) Theoretical and measured l_{SPP} versus λ with error bars denoting the standard error of the mean (SE).

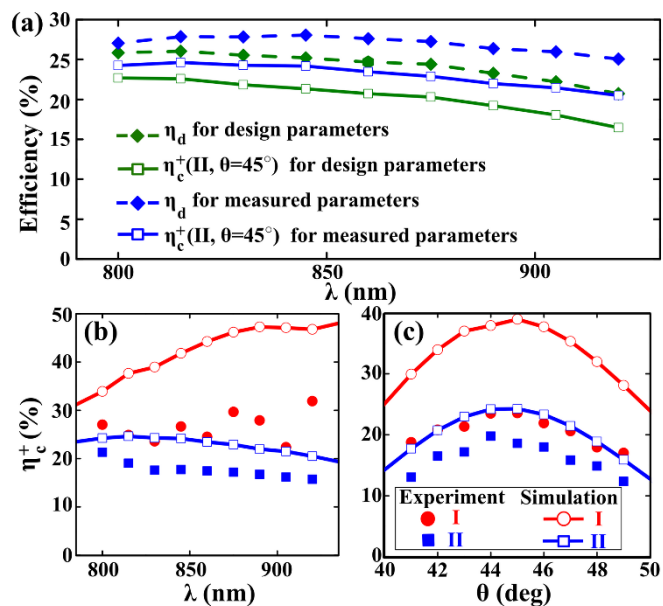


Figure 6 | (a) Numerical spectral behaviors of η_c^+ (II, $\theta=45^\circ$) and η_d calculated for the design parameters ($w = 120$ nm and $p = 480$ nm for both Launcher II and the decoupler) and the average measured parameters ($w = 105$ nm and $p = 495$ nm for Launcher II, and $w = 120$ nm and $p = 499$ nm for the decoupler). (b)(c) Experimental and a-FMM calculated η_c^+ versus λ at $\theta = 45^\circ$ (b), and versus θ at $\lambda = 830$ nm (c). The a-FMM calculations were performed with the average of measured slit parameters.

attached to a prism with index matching oil and then mounted on an XYZ linear translation plus Z axis rotation stage, so that the angle of incidence could be varied continuously. The decoupler, the launcher, and the iris's image reflected by the flat gold film are separately imaged onto a CCD using another imaging system composed of an objective O₂ (50×, NA = 0.5) and a lens L₂. Another calibrated vari-ND filter is placed in front of the CCD to keep the CCD away from saturation and to improve the signal-to-noise ratio (SNR) of obtained CCD images. To further improve the SNR, a spatial filter is used to block the reflection of the iris's image when the decoupler is imaged. This is because the re-radiation of the decoupler is very weak compared with the reflection of the iris's image without the spatial filter (see Fig. S2(c) in Supplementary Information). To measure the SPP propagation length, the sample is freestanding mounted. Normally incident light passed through the central slit launches bidirectional top-SPPs of the same intensities, which are scattered by the surrounding grooves (see inset in Fig. 5(a)). The re-radiations of both grooves are collected by another imaging system and imaged onto the CCD, whereas light that directly transmits through the slit is blocked by a spatial filtering system to improve the SNR.

CCD image processing. For the measurement of SPP launching efficiencies, the CCD images are processed as follows. The raw power of the re-radiation from the decoupler P_R is calculated by integrating the pixel intensities within the blue dashed box in Fig. 4(f), which is occupied by the decoupler and obtained via image edge recognition. The power of noise P_N is determined by adding the pixel intensities of the two yellow dashed boxes in Fig. 4(f). The yellow boxes located at the two sides of the decoupler are of the equal width but of half the length of the blue box. The noise-free radiation power is then obtained as $P_O = P_R - P_N$. The incident power P_{in} is obtained by measuring the reflection of the incident beam from flat gold film, i.e. integrating the pixel intensities in the same area as the white dashed box occupied by the launcher in Fig. 4(g). The white box occupied by the launcher is also obtained via image edge recognition. Note that the calculation of P_O and P_{in} have taken into account the fact that CCD images of the decoupler and Launcher I are obtained using different transmission efficiencies of the calibrated vari-ND filter in front of the CCD, T_O and T_{in} , respectively. Taking into account that the decoupler is of half the length of the launcher, the total launching-decoupling efficiency incorporating the SPP propagation loss is written as $\eta^+ = \eta_c^+ \eta_d \exp(-l/l_{SPP}) = 2P_O/P_{in}$. The image processing for measuring the propagation length is similar. In Fig. 5(c), P_{r1} and P_{r2} are raw powers of the re-radiations from the grooves indicated by blue dashed boxes, which are extracted via image edge recognition. The noises powers P_{n1} and P_{n2} are determined by adding the pixel intensities of the yellow-dashed boxes. The yellow boxes located at the two sides of the blue ones are of equal widths but are half the length of the blue boxes. As a result, $P_{g1} = P_{r1} - P_{n1}$ and $P_{g2} = P_{r2} - P_{n2}$ are the respective noise-free re-radiation powers from the left and right grooves. At every

wavelength, we fit the decay of the re-radiation power with an exponential to extract the top-SPP propagation length, i.e., $l_{SPP} = (d_2 - d_1)/(\ln P_{g1} - \ln P_{g2})$.

- Zia, R., Schuller, J. A., Chandran, A. & Brongersma, M. L. Plasmonics: the next chip-scale technology. *Mater. Today* **9**, 20–27 (2006).
- Ebbesen, T. W., Genet, C. & Bozhevolnyi, S. I. Surface-plasmon circuitry. *Phys. Today* **61**, 44–50 (2008).
- Gramotnev, D. K. & Bozhevolnyi, S. I. Plasmonics beyond the diffraction limit. *Nature Photon.* **4**, 83–91 (2010).
- Sorger, V. J., Oulton, R. F., Ma, R.-M. & Zhang, X. Toward integrated plasmonic circuits. *MRS Bulletin* **37**, 728–738 (2012).
- Zhao, C. & Zhang, J. Plasmonic demultiplexer and guiding. *ACS Nano* **4**, 6433–6438 (2010).
- Li, L., Li, T., Wang, S., Zhu, S. & Zhang, X. Broad band focusing and demultiplexing of in-plane propagating surface plasmons. *Nano Lett.* **11**, 4357–4361 (2011).
- Sorger, V. J., Lanzillotti-Kimura, N. D., Ma, R.-M. & Zhang, X. Ultra-compact silicon nanophotonic modulator with broadband response. *Nanophotonics* **1**, 17–22; DOI:10.1515/nanoph-2012-0009 (2012).
- Bouillard, J.-S., Vilain, S., Dickson, W., Wurtz, G. A. & Zayats, A. V. Broadband and broadangle SPP antennas based on plasmonic crystals with linear chirp. *Sci. Rep.* **2**, 829; DOI:10.1038/srep00829 (2012).
- Raether, H. *Surface plasmons on smooth and rough surfaces and on gratings* (Springer-Verlag, Berlin, 1988).
- Lopez-Tejiera, F. *et al.* Efficient unidirectional nanoslit couplers for surface plasmons. *Nature Phys.* **3**, 324–328 (2007).
- Baudrion, A.-L. *et al.* Coupling efficiency of light to surface plasmon polariton for single subwavelength holes in a gold film. *Opt. Express* **16**, 3420–3429; DOI:10.1364/OE.16.003420 (2008).
- Ferry, V. E., Sweatlock, L. A., Pacifici, D. & Atwater, H. A. Plasmonic nanostructure design for efficient light coupling into solar cells. *Nano Lett.* **8**, 4391–4397 (2008).
- Liu, H., Lalanne, P., Yang, X. & Hugonin, J.-P. Surface plasmon generation by subwavelength isolated objects. *IEEE J. Sel. Top. Quant. Electron.* **14**, 1522–1529 (2008).
- Wang, B. *et al.* Efficient generation of surface plasmon by single-nanoslit illumination under highly oblique incidence. *Appl. Phys. Lett.* **94**, 011114 (2009).
- Chen, J. *et al.* Broadband unidirectional generation of surface plasmon polaritons with dielectric-film-coated asymmetric single-slit. *Opt. Express* **19**, 26463–26469; DOI:10.1364/OE.19.026463 (2011).
- Liu, Y. *et al.* Compact magnetic antennas for directional excitation of surface plasmons. *Nano Lett.* **12**, 4853–4858 (2012).
- Liao, H. *et al.* A submicron broadband surface-plasmon-polariton unidirectional coupler. *Sci. Rep.* **3**, 1918; DOI:10.1038/srep01918 (2013).
- Baron, A. *et al.* Compact antenna for efficient and unidirectional launching and decoupling of surface plasmons. *Nano Lett.* **11**, 4207–4212 (2011).
- Lévéque, G. & Martin, O. J. F. Optimization of finite diffraction gratings for the excitation of surface plasmons. *J. Appl. Phys.* **100**, 124301 (2006).
- Laluet, J. Y. *et al.* Optimization of surface plasmons launching from subwavelength hole arrays: modelling and experiments. *Opt. Express* **15**, 3488–3495; DOI:10.1364/OE.15.003488 (2007).
- Bonod, N., Popov, E., Li, L. & Chernov, B. Unidirectional excitation of surface plasmons by slanted gratings. *Opt. Express* **15**, 11427–11432; DOI:10.1364/OE.15.011427 (2007).
- Bai, B. *et al.* Asymmetrical excitation of surface plasmon polaritons on blazed gratings at normal incidence. *Phys. Rev. B* **80**, 035407 (2009).
- Radko, I. P. *et al.* Efficient unidirectional ridge excitation of surface plasmons. *Opt. Express* **17**, 7228–7232; DOI:10.1364/OE.17.007228 (2009).
- Lu, J., Petre, C., Yablonovitch, E. & Conway, J. Numerical optimization of a grating coupler for the efficient excitation of surface plasmons at an Ag-SiO₂ interface. *J. Opt. Soc. Am. B* **24**, 2268–2272 (2007).
- Andkjær, J., Nishiwaki, S., Nomura, T. & Sigmund, O. Topology optimization of grating couplers for the efficient excitation of surface plasmons. *J. Opt. Soc. Am. B* **27**, 1828–1832 (2010).
- Huang, X. & Brongersma, M. L. Compact aperiodic metallic groove arrays for unidirectional launching of surface plasmons. *Nano Lett.* **13**, 5420–5424 (2013).
- Gao, H. *et al.* Rayleigh anomaly-surface plasmon polariton resonances in palladium and gold subwavelength hole arrays. *Opt. Express* **17**, 2334–2340; DOI:10.1364/OE.17.002334 (2009).
- Wang, B. & Lalanne, P. Surface plasmon polaritons locally excited on the ridges of metallic gratings. *J. Opt. Soc. Am. A* **27**, 1432–1441 (2010).
- Barnes, W. L., Murray, W. A., Dintinger, J., Devaux, E. & Ebbesen, T. W. Surface plasmon polaritons and their role in the enhanced transmission of light through periodic arrays of subwavelength holes in a metal film. *Phys. Rev. Lett.* **92**, 107401 (2004).
- Kim, D. S. *et al.* Microscopic origin of surface-plasmon radiation in plasmonic band-gap nanostructures. *Phys. Rev. Lett.* **91**, 143901 (2003).
- Lalanne, P., Hugonin, J.-P., Liu, H. & Wang, B. A microscopic view of the electromagnetic properties of sub-metallic surfaces. *Surf. Sci. Rep.* **64**, 453–469 (2009).



32. Li, G., Xiao, F., Cai, L., Alameh, K. & Xu, A. Theory of the scattering of light and surface plasmon polaritons by finite-size subwavelength metallic defects via field decomposition. *New J. Phys.* **13**, 073045; DOI:10.1088/1367-2630/13/7/073045 (2011).
33. Nagpal, P., Lindquist, N. C., Oh, S.-H. & Norris, D. J. Ultrasoft patterned metals for plasmonics and metamaterials. *Science* **325**, 594–597 (2009).
34. Lalanne, P. & Morris, G. M. Highly improved convergence of the coupled-wave method for TM polarization. *J. Opt. Soc. Am. A* **13**, 779–784 (1996).
35. Silberstein, E., Lalanne, P., Hugonin, J.-P. & Cao, Q. Use of grating theories in integrated optics. *J. Opt. Soc. Am. A* **18**, 2865–2875 (2001).
36. Palik, E. D. *Handbook of optical constants of solids* (Academic, New York, 1985).

Acknowledgments

We acknowledge P. Lalanne for the help on calculating the decoupling efficiency. This work was supported by the National Natural Science Foundation of China (Grant Nos. 61036005, 61377050, 61107065, and 11327902).

Author contributions

G.L. conceived the idea; J.Z. directed the project and designed the experiment; G.L. performed the simulation, fabrication and characterization. All authors analyzed the results, and contributed to the article.

Additional information

Supplementary information accompanies this paper at <http://www.nature.com/scientificreports>

Competing financial interests: The authors declare no competing financial interests.

How to cite this article: Li, G. & Zhang, J. Ultra-broadband and efficient surface plasmon polariton launching through metallic nanoslits of subwavelength period. *Sci. Rep.* **4**, 5914; DOI:10.1038/srep05914 (2014).



This work is licensed under a Creative Commons Attribution-NonCommercial-NoDerivs 4.0 International License. The images or other third party material in this article are included in the article's Creative Commons license, unless indicated otherwise in the credit line; if the material is not included under the Creative Commons license, users will need to obtain permission from the license holder in order to reproduce the material. To view a copy of this license, visit <http://creativecommons.org/licenses/by-nc-nd/4.0/>